

Cite this: *Environ. Sci.: Nano*, 2023, 10, 1897

Synergistic effect of exposed facets and surface defects of ZnO nanomaterials for photocatalytic ozonation of organic pollutants†

Yang Yang,^a Junmin Peng,^a Huilin Tao,^{ab} Zhou Yang,^a Yidong Hou,^{iD}*^a
Wei Lin,^{iD}*^a and Jinshui Zhang,^{iD}*^a

The development of efficient catalysts is of great significance in the photocatalytic ozonation process for organic wastewater treatment. However, the effect of exposed facets and surface defects of the catalyst on the photocatalytic ozonation performance is less covered. Herein, ZnO nanocomposites with different preferentially exposed crystal facets (ZnO-rod and ZnO-disk) were synthesized and used for photocatalytic ozonation of phenol. The characterization and density functional theory calculation results demonstrated that the exposed {0001} facets and oxygen vacancies promoted the separation and transfer of photogenerated charges as well as improved the adsorption and activation of ozone molecules on the catalyst surface. Consequently, the TOC removal rate in the UV-O₃/ZnO-disk process (62.4%) was much higher than those in the UV-O₃/ZnO-rod process (41.3%) and the UV-O₃ process (15%). Moreover, the experimental results of the identification and quenching of active species illustrated that ·OH was more likely to be produced in the UV-O₃/ZnO-disk process, while ¹O₂ was more likely to be formed over ZnO-rod. A large amount of ·OH with a stronger oxidation capability than ¹O₂ contributed to the superiority of ZnO-disk over ZnO-rod in organic pollutant removal. This work demonstrates that the engineering of crystal facets and surface defects provides an effective strategy for constructing efficient catalysts for the photocatalytic ozonation process.

Received 16th April 2023,
Accepted 17th May 2023

DOI: 10.1039/d3en00235g

rsc.li/es-nano

Environmental significance

The development of efficient catalysts is of great significance in the photocatalytic ozonation process for organic wastewater treatment. However, the study on the effect of exposed facets and surface defects of the catalyst on the photocatalytic ozonation performance is quite limited. In the present work, as a prototypical catalyst, ZnO with different exposed crystal facets and surface defects was prepared and applied to the photocatalytic ozonation of phenol. It was found that ZnO triggered a significant synergy between photocatalysis and ozonation, and ZnO-disk exhibited a much higher reactivity in phenol mineralization than ZnO-rod. This could be due to the synergetic effect of exposed facets and surface defects (O_v) on the basis of the characterization and density functional theory calculation results. This work not only provides some insight into the production of reactive oxygen species in the reaction but also provides some guidance in designing and constructing efficient catalysts for the photocatalytic ozonation process.

1. Introduction

Rapid industrialization has resulted in the massive discharge of organic pollutants, which will pose a threat to the aquatic ecosystem; thus the development of efficient strategies to remove refractory organic contaminants has aroused extensive attention in recent years.^{1,2} Photocatalysis has been proven to be an effective and mild way to degrade

pollutants, but its efficiency is moderate due to the high recombination rate of photogenerated carriers.^{3,4} Although the ozonation process exhibits a rapid organic degradation rate in some cases, its application is still limited by its poor mineralization to some extent.^{5,6} The combination of photocatalysis and ozonation has been reported to be a promising approach to solve the aforementioned problems.^{7,8} Since ozone has strong electrophilicity, the introduction of ozone into the photocatalysis process not only promotes the separation of photogenerated carriers and improves the photocatalytic reaction efficiency but also rapidly transforms ozone into active oxygen species and increases the utilization rate of ozone.^{9–12} However, the actual efficiency in the combined oxidation process is not as satisfactory as expected in many cases because the

^a State Key Laboratory of Photocatalysis on Energy and Environment, College of Chemistry, Fuzhou University, Fuzhou, 350002, People's Republic of China.

E-mail: ydhou@fzu.edu.cn, wlin@fzu.edu.cn, Jinshui.Zhang@fzu.edu.cn

^b School of Chemistry and Environmental Science, Shangrao Normal University, Shangrao, 334001, People's Republic of China

† Electronic supplementary information (ESI) available. See DOI: <https://doi.org/10.1039/d3en00235g>

photocatalyst cannot effectively activate ozone. Therefore, it is of great significance to develop efficient catalysts for the photocatalytic ozonation process.

In a heterogeneous catalytic reaction, the various types and states of exposed atoms of the catalyst surface significantly influence the formation of reactive sites, the adsorption-desorption processes, and the transformation mechanism of reactant molecules.^{13–15} For anisotropic semiconductor nanocomposites, crystal facet engineering was used to regulate the adsorption and activation of ozone molecules on the catalyst surface.^{16,17} For example, MnO₂ nanorods with exposed {310} facets contained abundant defect sites, which were beneficial to the adsorption and activation of ozone molecules, resulting in good catalytic ozonation for organic wastewater treatment.¹⁸ Semiconductor nanomaterials often have plenty of defects on their surface, which facilitate the adsorption and activation of ozone.^{19–21} In fact, exposed crystal facets and surface defects are closely related in nanomaterials. For example, the catalyst's predominantly exposed crystal facets have high surface energy, and defects are easily formed on its surface, thus the effects of crystal facets and surface defects on ozone activation are coexisting or synergistic.¹⁶ Additionally, crystal facets and surface defects significantly affect the direction and rate of the photogenerated charge migration for a certain photocatalyst, greatly influencing the photocatalytic activity.^{22–26} Inspired by this, we speculated that the simultaneous engineering of exposed facets and surface defects could optimize the surface structure of the catalyst, which will improve the interaction between ozone and the catalyst. This could promote the photocatalytic activation of ozone and realize the effective coupling of photocatalysis and ozonation.

Among the various catalysts for the photocatalytic ozonation process, ZnO can behave as both a photocatalyst and an ozonation catalyst, and it has been widely used in environmental remediation.^{27–29} Moreover, wurtzite ZnO contains an alternating arrangement of Zn²⁺ and O²⁻ ions along the *c*-axis, and its surface structure (especially exposed crystal facets and surface defects) can be regulated easily.^{30–32} For these reasons, ZnO was selected as the prototypical catalyst to explore the effect of exposed facets and surface defects on the photocatalytic ozonation process. Herein, ZnO nanomaterials with different exposed crystal facets and surface defects were prepared. In rod-like ZnO (ZnO-rod), the {10 $\bar{1}$ 0} facet was mainly exposed, while disk-like ZnO (ZnO-disk) with exposed {0001} facets had abundant oxygen vacancies. ZnO-disk showed enhanced activity in the photocatalytic ozonation of organic pollutants, with a strong synergistic effect between photocatalysis and ozonation. Their crystal structure and morphology, together with their optical and electrochemical properties, were studied in detail. Meanwhile, the impact of exposed crystal facets and oxygen vacancies on ozone adsorption and activation was also systematically investigated. In combination with experiments on identification and quenching active species, we revealed the possible reaction mechanism for the UV-O₃/ZnO process toward organic removal.

2. Experimental

2.1 Materials

Zinc acetate dihydrate (Zn(CH₃COO)₂·2H₂O), phenol, 5,5-dimethyl-1-pyrroline-*N*-oxide (DMPO) and 2,2,6,6-tetramethyl-1-piperidinyloxy (TEMP) were purchased from Aladdin (China) Chemical Co., Ltd. Trisodium citrate dihydrate (Na₃C₆H₅O₇·2H₂O), *N,N*-dimethylformamide (DMF), sodium hydroxide (NaOH) and anhydrous ethanol were purchased from Sinopharm (China) Chemical Reagent Co., Ltd. All the chemicals were used without any further purification. Pure oxygen (Yuanhua Industrial Gases Co., Ltd., Fuzhou) was fed into an ozone generator (Anshan Technology, COM-AD) to produce ozone.

2.2 Synthesis of ZnO-disk and ZnO-rod

To synthesize ZnO-rod, 0.22 g Zn(CH₃COO)₂·2H₂O and 1.06 g Na₃C₆H₅O₇·2H₂O were dissolved in 50 mL ultra-pure water, and then 20 mL NaOH solution (2.0 mol L⁻¹) was added and stirred for 30 min. The mixture was put into an autoclave and heated at 200 °C for 12 h. After cooling to room temperature, the resulting precipitate was washed with water and ethanol, and dried in an oven at 80 °C overnight. The obtained solid was calcined at 300 °C for 1 h in a muffle furnace to remove the residual organic matter.

To synthesize ZnO-disk, 7.63 g Zn(CH₃COO)₂·2H₂O was dissolved in 50 ml ultra-pure water and 0.28 g NaOH was dissolved in another 20 ml ultra-pure water, respectively. The solutions were mixed and stirred for 30 min, and then the mixture was put into an autoclave and heated at 95 °C for 12 h. The subsequent processes were the same as those for ZnO-rod synthesis.

2.3 Catalyst characterization

The crystal phases of the ZnO products were identified by X-ray diffraction (XRD, Bruker D8 ADVANCE) with Cu K α radiation ($\lambda = 1.5406 \text{ \AA}$). The morphologies and microstructures were characterized by scanning electron microscopy (FESEM, Hitachi S4800) and transmission electron microscopy (TEM, Tecnai 20 FEG). The Brunauer-Emmett-Teller specific surface area (*S*_{BET}) was measured using MicroActive for the ASAP 2460 apparatus (USA). X-ray photoelectron spectroscopy (XPS) data were gathered using a PHI Quantum 2000 XPS with the C1s peak (284.6 eV) as a reference. Raman spectra were collected on a LabRAM HR Evolution Raman spectrometer. UV-vis diffuse reflectance spectra (DRS) of the samples were obtained using a Varian Cary 500 Scan. The Mott-Schottky plots and electrochemical impedance spectra (EIS) were collected with an electrochemical workstation (Bio-Logic SP-150), and the photocurrent was tested by using a PLS-SXE300 xenon lamp source (Beijing Perfectlight). The photoluminescence spectra (PL) and time-resolved transient photoluminescence decay spectra (TRPL) were analyzed using a Hitachi F900 fluorescence spectrophotometer. Electron paramagnetic

resonance (EPR) spectra were obtained using a Bruker model ESA A300 spectrometer.

2.4 Theoretical calculation

All the spin-polarized density functional theory (DFT) calculations were carried out by using the Vienna *ab initio* simulation package (VASP).^{33,34} The projector-augmented wave potentials were employed to describe the ion–electron interactions. The PBE functional was adopted to represent the exchange–correlation energy.³⁵ A computational model of four layers of ZnO was employed, in which the bottom two layers were constrained to maintain the bulk crystal structure, while the rest of the unit cells were allowed to relax. The unit cell also contained 15 Å of vacuum in the *z* direction. A cut-off energy of 500 eV was utilized for the expansion of the wave functions, and a Monkhorst–Pack mesh of $3 \times 3 \times 1$ also was adopted for *k*-sampling of the Brillouin zone. Moreover, the convergence criteria for the energy and force were set to 1×10^{-5} eV per atom and 0.02 eV Å⁻¹, respectively.

2.5 Analytical methods

In a typical photocatalytic ozonation process, the reactor consisted of a 160 mL suspension of 50 mg L⁻¹ phenol and 0.5 g L⁻¹ catalyst, and four UV lamps (Philips, TUV 6W G6T5, 365 nm) were placed around it as the light source. At the same time, ozone was injected at a flow rate of 50 mL min⁻¹ and a concentration of 10 mg L⁻¹ (Fig. S1†). During the operation, a specific volume of solution was extracted from the reactor every 20 minutes for analysis. The phenol concentration was determined using an LC-15C HPLC (Shimadzu, Japan), and the total organic carbon (TOC) was determined using a Shimadzu TOC-VCPH analyzer. Finally, the experiments of photocatalysis, ozonation, and adsorption were separately carried out under identical conditions as comparison experiments. All experiments were stirred in the dark for 0.5 h before the reaction to achieve adsorption–desorption equilibrium.

3. Results and discussion

3.1 Crystal structure and morphology

Fig. 1a shows the XRD patterns of the samples; the peaks can be indexed well to hexagonal wurtzite ZnO (JCPDS No. 36-1451). No diffraction peaks from any other impurities are observed. However, the difference in the relative peak intensities of the samples is quite distinct. ZnO-rod displays the strongest peak of the (100) plane, while ZnO-disk displays the strongest peak of the (002) plane. This could be closely related to the exposed crystal facets in the sample. The higher intensity ratio ($I_{(002)}/I_{(100)}$) of ZnO-disk means more exposure of {0001} facets in the sample.^{36,37} Fig. 1b and c show typical SEM images of ZnO-disk and ZnO-rod. ZnO-disk exhibits a symmetrical hexagon with a length and thickness

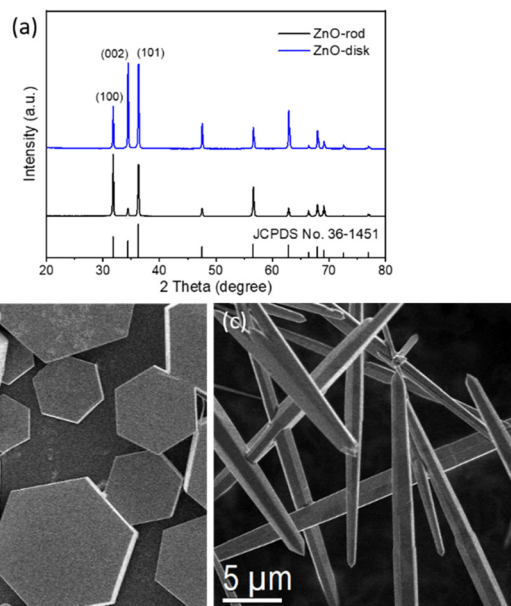


Fig. 1 (a) XRD patterns and (b and c) SEM images for the as-prepared ZnO.

of several micrometers, while ZnO-rod consists of rods with a length of a dozen micrometers.

The catalysts were further characterized by TEM and HRTEM. As seen in Fig. 2a and d, ZnO-rod and ZnO-disk distinctly show disk-like and rod-like morphologies, respectively, which is consistent with the SEM results. The HRTEM image in Fig. 2b shows that the spacing of the lattice fringes in ZnO-rod is measured to be 0.26 nm, which indicates that ZnO-rod grows along the *c* axis ([0001]). Meanwhile, the SAED image taken along the [01 $\bar{1}$ 0] zone axis proves that ZnO-rod takes precedence over the exposed {10 $\bar{1}$ 0} facets (Fig. 2c). As shown in Fig. 2e, the lattice fringe spacing of ZnO-disk is 0.28 nm, corresponding to the (100) plane of wurtzite ZnO. The selected area electron diffraction (SAED) mode pattern can be indexed as the [0001] region of the single-crystal hexagonal ZnO zone axis (Fig. 2f),

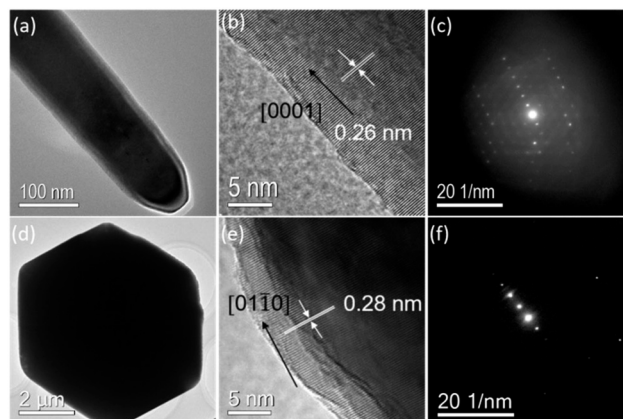


Fig. 2 (a and d) TEM images, (b and e) HRTEM images, and (c and f) SAED images for ZnO-rod and ZnO-disk.

indicating that the exposed crystal facet is {0001}. Their S_{BET} values were also determined by N_2 -adsorption measurements, and both ZnO-disk and ZnO-rod have very low values (0.4 and $0.7 \text{ m}^2 \text{ g}^{-1}$, Fig. S2†). Therefore, the effect of specific surface area on the catalytic activity can be ignored in this study.

3.2 Surface analysis

XPS spectroscopy was carried out to investigate the elemental composition and chemical state of the samples. In Fig. S3,† ZnO-disk and ZnO-rod show two sharp peaks located at 1021.6 eV and 1044.6 eV, corresponding to Zn $2p_{3/2}$ and Zn $2p_{1/2}$. The O 1s spectra (Fig. 3a) can be fitted into three peaks by Gaussian distribution to better understand the variation of oxygen states.^{38,39} The lower binding energy peak (O_I) centered at 530.4 eV is ascribed to the lattice oxygen in the hexagonal wurtzite structure. The higher binding energy (O_{III}) at 532.1 eV is related to the chemisorbed oxygen and water from atmospheric contamination. The middle O_{II} peak located at 531.6 eV is assigned to the oxygen vacancy (O_V) of ZnO, and the peak intensity is associated with the O_V concentration in the sample. The quantitative analysis results for the O 1s spectra are summarized in Table S1.† The O_{II} peak area ratio in ZnO-disk reaches 0.21, indicating that its surface has abundant O_V , while the O_{II} peak area ratio in ZnO-rod is only 0.13. The significant difference in O_{II} content for the ZnO samples also implies the significant difference in their surface structures.

The Raman technique was employed to further study the defects in the samples. In Fig. 3b, three characteristic Raman peaks of wurtzite-phase ZnO appear at 330, 380 and 437 cm^{-1} , assigned to $E_{2(\text{High})}$ - $E_{2(\text{Low})}$, the transverse optical vibration (TO) of A_1 and $E_{2(\text{High})}$ modes, respectively.³¹ The peak at 437 cm^{-1} reflects the structural integrity and phase homogeneity. Notably, the peak centered at 585 cm^{-1} is assigned to the $E_{1(\text{Low})}$ model, which is related to the O_V of

ZnO.^{40,41} Comparing the peak intensity of the two samples further confirms that the O_V concentration in ZnO-disk is higher than that in ZnO-rod.

EPR spectroscopy was carried out to study the defects and electronic states of the samples under different conditions. In Fig. 3c, no apparent signal is observed over ZnO-rod, and no change is found after introducing light and/or ozone. However, ZnO-disk displays a clear signal near $g = 2.003$ under dark conditions, which is commonly ascribed to shallow donors caused by singly ionized O_V .^{37,42} In general, the presence of O_V can effectively trap the photogenerated electrons, which is confirmed by the enhanced signal over ZnO-disk under light irradiation. After introducing ozone, the signal intensity becomes lower than the initial intensity. The decrease in signal intensity could be attributed to the transfer of free electrons from the defects to ozone molecules. According to these results, it can be deduced that the presence of O_V is beneficial for activating ozone, which will accelerate the photocatalytic ozonation process.

3.3 Density functional theory (DFT)

DFT calculations were performed to understand the surface properties and ozone adsorption behavior on different crystal facets of ZnO (Fig. S4†). The surface energy, oxygen vacancy formation energy, and ozone adsorption energy over different crystal facets are summarized in Table 1. The surface energy of {0001} (Zn-terminated plane, 1.89 J m^{-2}) is close to that of {000 $\bar{1}$ } (O-terminated plane, 1.88 J m^{-2}), which is greater than that of non-polar plane {10 $\bar{1}0$ } (1.40 J m^{-2}). In general, surface defects prefer to form on a plane with high surface energy.^{43–47} As expected, the lowest oxygen vacancy formation energy (6.34 eV) is obtained over {000 $\bar{1}$ } of ZnO, meaning that an oxygen vacancy is easily formed over ZnO-disk, which is consistent with the XPS and EPR results. The ozone adsorption over {0001} (-3.45 eV) is much stronger than those over {000 $\bar{1}$ } (-1.25 eV) and {10 $\bar{1}0$ } (-1.16 eV), indicating that O_3 adsorption tends to occur more on the {0001} facet with exposed Zn atoms. Considering that ZnO-disk has abundant O_V on {000 $\bar{1}$ } facets, we also constructed ZnO surfaces with oxygen defects and investigated O_3 adsorption on the plane surface. The ozone adsorption over {000 $\bar{1}$ } with O_V (-4.85 eV) is much stronger than that over a perfect plane surface. It can be concluded that O_3 readily adsorbs on {0001} facets rather than on {000 $\bar{1}$ } and {10 $\bar{1}0$ } plane surfaces. The presence of oxygen vacancies on the {000 $\bar{1}$ } plane facilitates ozone adsorption. The adsorbed O_3 will undergo

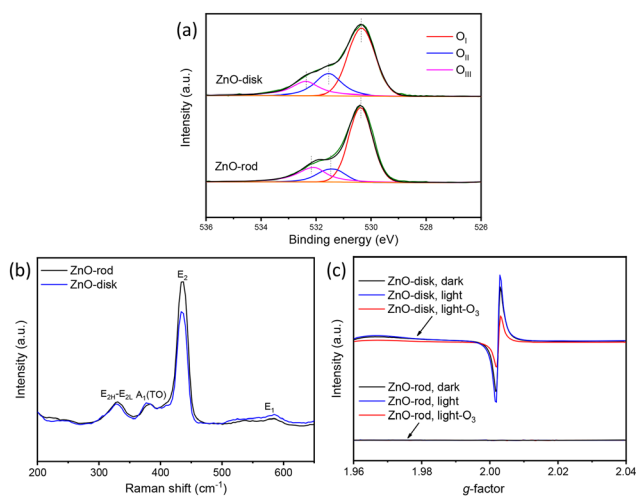


Fig. 3 (a) High-resolution O 1s XPS spectra, (b) Raman spectra and (c) EPR signals for ZnO-rod and ZnO-disk.

Table 1 Surface energy (E_{surf}), ozone adsorption energy (E_{ads}), oxygen vacancy formation energy (E_{O_V}), and the energy of ozone adsorption on the oxygen vacancy surface ($E_{\text{ads}}(\text{O}_V)$) over different crystal facets of ZnO

	$E_{\text{surf}}/\text{J m}^{-2}$	E_{ads}/eV	E_{O_V}/eV	$E_{\text{ads}}(\text{O}_V)/\text{eV}$
{0001}-Zn	1.89	-3.49	7.71	-4.85
{000 $\bar{1}$ }-O	1.88	-1.25	6.34	-2.27
{10 $\bar{1}0$ }	1.40	-1.16	7.39	-3.32

further activation cleavage to produce reactive oxygen radicals and participate in the photogenerated electron-hole pairs in the photocatalytic ozonation process.

3.4 Optical properties and band structure

The UV-vis diffusion reflectance spectra for the samples are shown in Fig. 4a. The two samples exhibit a distinct absorption edge at around 400 nm, which is caused by the bandgap transition.⁴⁸ The band gap energy can be estimated from the Tauc plots of $\{(F(R) \times hv)^2\}$ to photon energy (hv) (Fig. 4a), and its value is about 3.2 eV. Mott-Schottky curves were measured to determine the conduction band position of the samples. In Fig. 4b and c, the positive slope of the linear plots illustrates the characteristic behavior of an n-type semiconductor, and the flat band potentials for ZnO-rod and ZnO-disk are -0.35 and -0.30 V vs. NHE, respectively. For an n-type semiconductor, the conduction band potential is 0.1 V lower than the flat-band potential, thus the conduction band positions for ZnO-rod and ZnO-disk are -0.45 and -0.40 V vs. NHE, respectively. In combination with the band gap energy, their band structure is present in Fig. 4d, and ZnO-disk and ZnO-rod show similar redox potentials of electron-hole pairs. Since the redox potentials of O_3/O_3^- and OH/OH^- are 1.6 V and 2.38 V, respectively, the conduction and valence band positions of ZnO are thermodynamically capable of producing reactive oxidation species (ROS).

3.5 Charge separation and transfer

The photogenerated charge separation and transfer properties of the samples were investigated by the PL technique, impedance spectroscopy, and photocurrent tests. In Fig. 5a, the PL spectrum is mainly composed of the ultraviolet region and visible region (480–650 nm). The peak at 386 nm can be assigned to the radiative transition of the electron from the conduction band to the valence band.⁴⁹

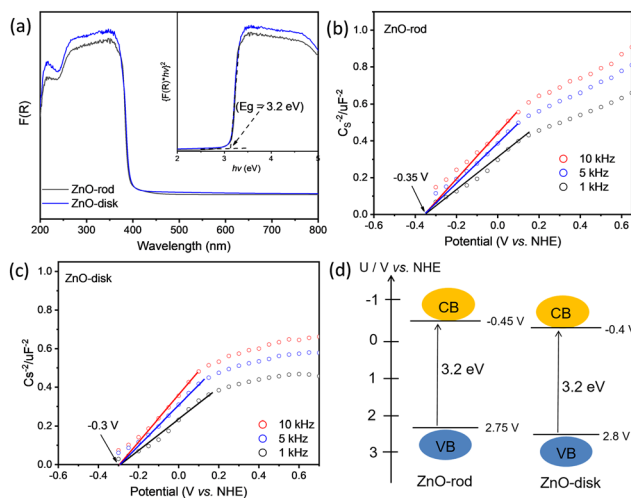


Fig. 4 (a) DRS spectra (inset: the Kubelka-Munk transformation), (b) and (c) Mott-Schottky plots and (d) schematic energy band structures for ZnO-rod and ZnO-disk.

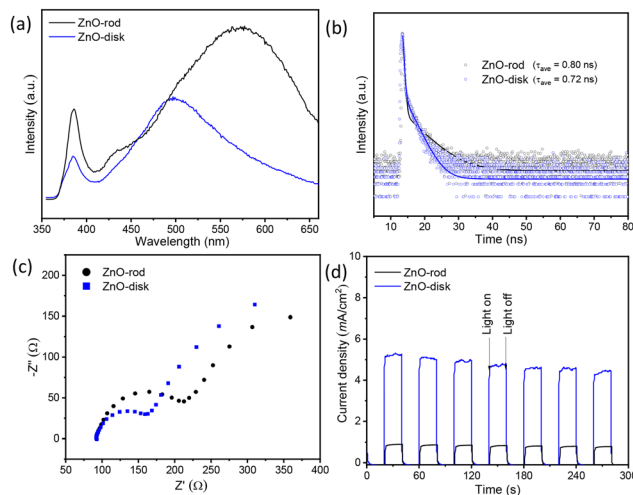


Fig. 5 (a) PL spectra, (b) TRPL decay spectra, (c) EIS Nyquist plots and (d) photocurrent responses for ZnO-rod and ZnO-disk.

The lower PL intensity in ZnO-disk indicates that it has lower recombination of photogenerated electron-hole pairs than ZnO-rod. According to a report, the broad band in the visible region is related to different defects in the crystal structure of ZnO, such as O_V , V_{Zn} , O_i , and extrinsic impurities.⁵⁰ In regard to ZnO-rod, the broad band centred at about 570 nm is correlated with O_i . ZnO-disk has a band at 500 nm assigned to O_V , which may be caused by radiative recombination of generated holes with electrons belonging to singly ionized O_V .^{51,52} As shown in the TRPL spectra (Fig. 5b), the average lifetime (0.72 ns) of ZnO-disk is shorter than that of ZnO-rod (0.8 ns), further confirming the higher efficiency of the photogenerated charge separation over ZnO-disk.⁵³ Fig. 5c shows the EIS Nyquist plots of the ZnO samples, ZnO-disk has a smaller arc radius, indicating a better charge transfer efficiency over ZnO-disk. Additionally, the photocurrent responses for ZnO-disk and ZnO-rod were measured. In Fig. 5d, ZnO-disk exhibits a higher photocurrent than ZnO-rod, again implying a higher efficiency in the photogenerated charge separation and transfer over ZnO-disk, which could be partly ascribed to the internal electric field existing along the direction from $\{0001\}$ to $\{00\bar{1}\}$ as an intrinsic driving force.^{32,54} This is beneficial for forming reactive oxygen species in the photocatalytic ozonation process.

3.6 Degradation and mineralization of phenol

Since phenol compounds widely existing in wastewater have a stable molecular structure, poor biodegradability, and long-term residues, phenol was selected as the model organic pollutant to evaluate catalyst activity. In Fig. 6a, the degradation of phenol is negligible under UV light irradiation alone. The UV/ZnO process slightly degrades phenol, with 2% and 12% removal rates after 30 min for ZnO-rod and ZnO-disk, respectively. The phenol removal can reach 69% in the ozonation process after 30 min. The degradation rate increases to 74% in the UV- O_3 process. After introducing ZnO

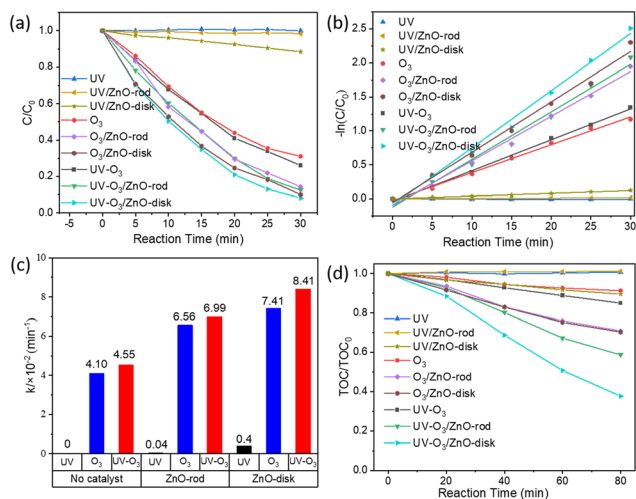


Fig. 6 (a) The degradation rates, (b) pseudo first-order kinetics fitting, (c) pseudo first-order reaction constants and (d) TOC removal in the different processes for phenol degradation.

in the UV-O₃ process, the degradation rate increases to a certain degree. However, no significant change is observed between the ozonation process and the photocatalytic ozonation process because O₃ can swiftly destroy phenol and complete removal can be achieved within a short time.⁵⁵ To better compare the different processes, the pseudo-first-order kinetics was well-fitted for phenol degradation (Fig. 6b). In the UV-O₃/ZnO-disk process, the first-order rate constant (k) is $8.41 \times 10^{-2} \text{ min}^{-1}$, which is much higher than that in the UV-O₃ process ($4.55 \times 10^{-2} \text{ min}^{-1}$), indicating that ZnO has good photocatalytic ozonation activity. The k values for the photocatalytic, ozonation, and photocatalytic ozonation degradation processes are summarized in Fig. 6c. The magnitude of the k values follows the order UV-O₃/ZnO > O₃/ZnO > UV-O₃ > O₃ > UV/ZnO > UV, indicating that photocatalytic ozonation is the most efficient process for degrading phenol. In particular, the k value of photocatalytic ozonation is greater than the sum of those of photocatalysis and ozonation, indicating that it has a synergistic effect in the photocatalytic ozonation process. However, the ozonation process usually results in many intermediates of organic pollutants, leading to unsatisfactory TOC removal.

The TOC changes in the different processes were further monitored. In Fig. 6d, the TOC removal is negligible in the process of UV or UV/ZnO-rod, and a TOC removal rate of 10.5% is achieved in the process of UV/ZnO-disk after 80 min. This suggests that ZnO-disk has a better photocatalytic mineralization ability than ZnO-rod. In the case of single ozonation, the TOC removal is only 8.7%. The TOC removal rate increases to a certain degree in the process of UV-O₃. The TOC removal rates in the O₃/ZnO-disk and O₃/ZnO-rod processes are comparable, and the values are about 30%. Surprisingly, when ozonation and photocatalysis are combined, the TOC removal rate is significantly enhanced. The UV-O₃/ZnO-disk process exhibits the best performance with a 62.4% TOC removal rate, which is much higher than

UV-O₃/ZnO-rod (41.3%) and UV-O₃ (15%). According to the phenol mineralization results, the UV-O₃/ZnO process is superior to the sum of O₃/ZnO and UV/ZnO processes. This illustrates that ZnO triggers a synergistic effect between photocatalysis and ozonation. ZnO-disk and ZnO-rod exhibit different activities in the photocatalytic ozonation for phenol mineralization, possibly due to the different amounts of ROS produced in the reaction system.

3.7 Reaction mechanism

The ROS produced in the photocatalytic ozonation process was studied by EPR trapping experiments. Hydroxyl radical ($\cdot\text{OH}$) and superoxide radical ($\cdot\text{O}_2^-$) signals were detected by using DMPO as the spin marker in aqueous and methanol solutions, respectively. A singlet oxygen radical ($^1\text{O}_2$) signal was detected by using TEMP as the spin marker in aqueous solution. In Fig. 7a, the $\cdot\text{OH}$ signal is barely observed in the UV-O₃ process. However, a typical signal of DMPO- $\cdot\text{OH}$ adducts with an intensity ratio of 1:2:2:1 is detected after adding the ZnO catalyst, and the signal for ZnO-disk is much stronger than that for ZnO-rod, which confirms that ZnO-disk can generate much more $\cdot\text{OH}$ than ZnO-rod in the photocatalytic ozonation process. In Fig. 7b, a typical DMPO- $\cdot\text{O}_2^-$ adduct signal with an intensity ratio of 1:1:1:1 is observed in the UV-O₃ and UV-O₃/ZnO processes. Surprisingly, the $\cdot\text{O}_2^-$ signal in the UV-O₃ process is much stronger than those of UV-O₃/ZnO-rod and UV-O₃/ZnO-disk, which indicates that O₃ reacts more quickly to form $\cdot\text{O}_2^-$ under UV light irradiation. With the addition of ZnO, the generation of $\cdot\text{O}_2^-$ is inhibited, implying that O₃ is more easily converted into other reactive oxygen radicals, such as $\cdot\text{OH}$. Fig. 7c shows typical signals of TEMP- $^1\text{O}_2$ adducts with an intensity ratio of 1:1:1 detected in all cases. Interestingly, the $^1\text{O}_2$ signal of UV-O₃/ZnO-rod is stronger than those of UV-

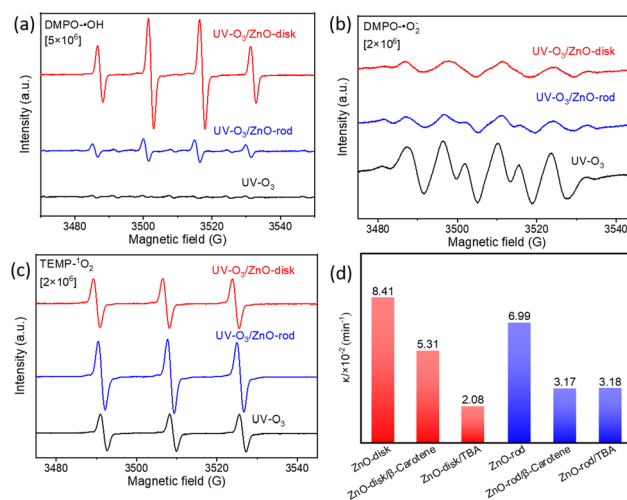


Fig. 7 (a-c) EPR spectra of DMPO- $\cdot\text{OH}$, DMPO- $\cdot\text{O}_2^-$ and TEMP- $^1\text{O}_2$ in the different processes; (d) comparison of pseudo first-order reaction constants for phenol removal in the presence of different radical scavengers.

O_3 and UV- O_3 /ZnO-disk, indicating that 1O_2 is more likely to be generated in the UV- O_3 /ZnO-rod process. In the dark, the 1O_2 signal of O_3 , O_3 /ZnO-rod or O_3 /ZnO-disk is feeble (Fig. S5[†]). Based on the above analysis, it can be deduced that under light irradiation and in the presence of ozone, the ROS generated over ZnO nanomaterials with different exposed facets vary. $\cdot OH$ is more likely to be produced over ZnO-disk, while 1O_2 is more likely to be generated over ZnO-rod.

A series of capturing experiments were carried out to examine the role of the ROS produced in phenol degradation. *tert*-Butanol (*t*BA) and β -carotene were used as $\cdot OH$ and 1O_2 scavengers, respectively. Considering that the use of *t*BA and β -carotene increases the TOC value of a solution, the degradation rate was adopted as an index to investigate the change after adding a scavenger. As shown in Fig. 7d, in the process of UV- O_3 /ZnO-disk, both *t*BA and β -carotene are found to inhibit phenol degradation, in which *t*BA shows a more significant inhibiting effect. This means that $\cdot OH$ is the dominated ROS in the degradation of phenol for the UV- O_3 /ZnO-disk process. In the case of UV- O_3 /ZnO-rod, *t*BA exhibits a similar suppression effect to β -carotene in the degradation of phenol, indicating that both $\cdot OH$ and 1O_2 contribute to the phenol degradation.

According to the above analysis, a possible mechanism for phenol removal in the UV- O_3 /ZnO process was proposed (Fig. 8). First, photogenerated electrons and holes are generated and transferred to the surface of ZnO under UV light irradiation. Since the valence band (VB) potential of ZnO is about 2.8 V vs. NHE, pH = 7, which is more positive than $\cdot OH/H_2O$ (2.38 V vs. NHE, pH = 7), the photogenerated hole can directly oxidize water to generate $\cdot OH$ (eqn (5)). However, the conduction band (CB) potential of ZnO (-0.4 V vs. NHE) is very close to the redox potential of $O_2/O_2^{\cdot -}$ (-0.33 V vs. NHE); thus the photogenerated electrons cannot smoothly transfer to dissolved oxygen in solution. This certainly influences the utilization of photogenerated carriers and the generation of ROS (such as h^+ , $\cdot OH$, and 1O_2) in the photocatalytic system. When ozone with strong electrophilicity is introduced into the photocatalytic system, it can rapidly capture the photogenerated electrons on the CB and form an ozone radical ($\cdot O_3^{\cdot -}$) (eqn (2)), which generates $\cdot OH$ through a radical chain reaction (eqn (3)–(4)).

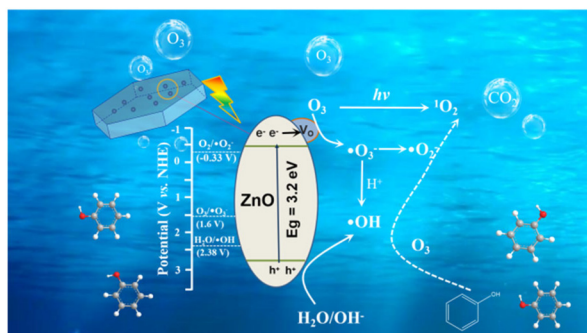
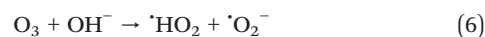


Fig. 8 Possible reaction mechanism for phenol removal in the UV- O_3 /ZnO process.

Similarly, ozone dissolved in solution directly reacts with OH^- to form $\cdot O_2^{\cdot -}$ (eqn (6)). 1O_2 is most likely generated by two pathways: (i) dissociation of O_3 (eqn (7)) and (ii) $\cdot O_2^{\cdot -}$ oxidation by holes (eqn (8)).^{7,56–60}



In the case of ZnO-disk, the {0001} polar facets are predominately exposed, where the internal electric field is intrinsically established, leading to the efficient separation of the electron-hole pairs. Additionally, the presence of abundant O_v in ZnO-disk can effectively adsorb and activate ozone, thus improving the ozone utilization in the UV- O_3 /ZnO process (Fig. S6[†]). Moreover, ZnO-disk has much better hydrophilicity than ZnO-rod (Fig. S7[†]); thus the generated hole readily reacts with hydroxyl groups and/or water on the surface to produce $\cdot OH$. However, due to its more hydrophobic surface, the photogenerated holes are more likely to react with $\cdot O_2^{\cdot -}$ to produce 1O_2 over ZnO-rod. Therefore, the produced $\cdot OH$ with high oxidation capability results in the efficient mineralization of organic pollutants in the UV- O_3 /ZnO-disk process.

3.8 Stability and universality

There is no doubt that stability is an essential index for the evaluation of catalysts in practical applications. After

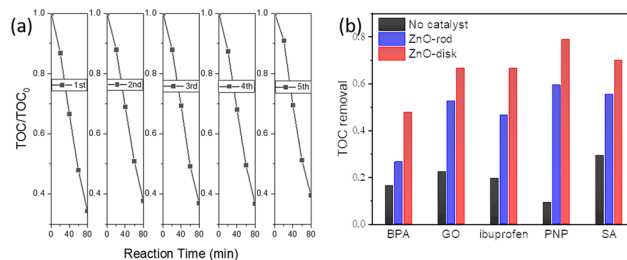


Fig. 9 (a) Reusability of ZnO-disk and (b) TOC removal in photocatalytic ozonation of different organic pollutants (conditions: $[O_3] = 10 \text{ mg L}^{-1}$, [catalyst] = 0.5 g L^{-1} reaction temperature = $25 \text{ }^\circ\text{C}$, reaction time = 80 min, [BPA] = 50 mg L^{-1} , [GO] = 50 mg L^{-1} , [ibuprofen] = 20 mg L^{-1} , [PNP] = 50 mg L^{-1} , [SA] = 50 mg L^{-1}).

each cycling reaction, ZnO-disk was recycled by centrifuging and washing with deionized water. In Fig. 9a, no noticeable deactivation is observed in the cyclic runs, and the TOC removal phenol slightly decreases from 65.8% to 61.2% after five runs. Meanwhile, the XRD patterns and SEM images of the used ZnO-disk were studied. In Fig. S8,† there is no noticeable difference between fresh and used samples. All these results confirm the good stability of ZnO-disk in the photocatalytic ozonation process for phenol removal.

To assess whether the catalyst is universal or solely selective in the mineralization of organics, we also applied ZnO catalysts to remove several other typical organics such as bisphenol A (BPA), golden orange II (GO), ibuprofen, *p*-nitrophenol (PNP) and salicylic acid (SA). Fig. 9b clearly illustrates that introducing ZnO boosts the TOC removal rate, particularly in removing ibuprofen and PNPP. It makes sense to widen the application of the as-prepared ZnO for the mineralization of various organics.

4. Conclusions

In summary, we synthesized two kinds of ZnO nanomaterials with different preferentially exposed facets (ZnO-rod and ZnO-disk) and applied them to photocatalytic ozonation of organic pollutants. The results indicated that ZnO triggered a significant synergy between photocatalysis and ozonation, and ZnO-disk exhibited a much higher reactivity in phenol mineralization than ZnO-rod. This could be due to the synergetic effect of the exposed facets and surface defects (O_V). Most notably, EPR spectroscopy and free radical scavenging experiments explain well the differences in the production of ROS over ZnO-disk and ZnO-rod in the photocatalytic ozonation process. In addition, ZnO-disk also exhibited good stability and broad universality in removing organic pollutants. This fundamental study can pave a new avenue for the architecture of highly efficient catalysts and the development of photocatalytic ozonation for organic pollutant elimination.

Conflicts of interest

There are no conflicts of interest to declare.

Acknowledgements

This work was supported by the NSFC (22072021, 21972022, and U21A20326), the National Key R&D Program of China (2018YFA0209301), and the Award Program for Outstanding Young Innovative Talents of Fujian Province (00332111).

References

- 1 M. R. Al-Mamun, S. Kader, M. S. Islam and M. Z. H. Khan, Photocatalytic activity improvement and application of UV-TiO₂ photocatalysis in textile wastewater treatment: a review, *J. Environ. Eng.*, 2019, 7, 103248.
- 2 L. Liu, Z. Chen, J. Zhang, D. Shan, Y. Wu, L. Bai and B. Wang, Treatment of industrial dye wastewater and pharmaceutical residue wastewater by advanced oxidation processes and its combination with nanocatalysts: a review, *J. Water Process. Eng.*, 2021, 42, 102122.
- 3 J. J. Rueda-Marquez, I. Levchuk, P. Fernández Ibañez and M. Sillanpää, A critical review on application of photocatalysis for toxicity reduction of real wastewaters, *J. Cleaner Prod.*, 2020, 258, 120694.
- 4 A. C. Mecha and M. N. Chollom, Photocatalytic ozonation of wastewater: a review, *Environ. Chem. Lett.*, 2020, 18, 1491–1507.
- 5 Y. Wang, X. Duan, Y. Xie, H. Sun and S. Wang, Nanocarbon-based catalytic ozonation for aqueous oxidation: engineering defects for active sites and tunable reaction pathways, *ACS Catal.*, 2020, 10, 13383–13414.
- 6 A. Aguinaco, F. J. Beltrán, J. F. García-Araya and A. Oropesa, Photocatalytic ozonation to remove the pharmaceutical diclofenac from water: influence of variables, *Chem. Eng. J.*, 2012, 189–190, 275–282.
- 7 Y. Jing, L. Li, Q. Zhang, P. Lu, P. Liu and X. Lu, Photocatalytic ozonation of dimethyl phthalate with TiO₂ prepared by a hydrothermal method, *J. Hazard. Mater.*, 2011, 189, 40–47.
- 8 F. J. Beltran and A. Rey, Solar or UVA-visible photocatalytic ozonation of water contaminants, *Molecules*, 2017, 22, 1177.
- 9 B. Lashuk and V. Yargeau, A review of ecotoxicity reduction in contaminated waters by heterogeneous photocatalytic ozonation, *Sci. Total Environ.*, 2021, 787, 147645.
- 10 M. Mehrjouei, S. Müller and D. Möller, A review on photocatalytic ozonation used for the treatment of water and wastewater, *Chem. Eng. J.*, 2015, 263, 209–219.
- 11 J. Wang and H. Chen, Catalytic ozonation for water and wastewater treatment: recent advances and perspective, *Sci. Total Environ.*, 2020, 704, 135249.
- 12 J. Xiao, Y. Xie and H. Cao, Organic pollutants removal in wastewater by heterogeneous photocatalytic ozonation, *Chemosphere*, 2015, 121, 1–17.
- 13 H. Li, J. Shi, K. Zhao and L. Zhang, Sustainable molecular oxygen activation with oxygen vacancies on the {001} facets of BiOCl nanosheets under solar light, *Nanoscale*, 2014, 6, 14168–14173.
- 14 S. Boochakiat, D. Tantraviwat, O. Thongsook, S. Pornsuwan, A. Nattestad, J. Chen, D. Channei and B. Inceesungvorn, Effect of exposed facets of bismuth vanadate, controlled by ethanolamine, on oxidative coupling of primary amines, *J. Colloid Interface Sci.*, 2021, 602, 168–176.
- 15 H. Li, J. Li, Z. Ai, F. Jia and L. Zhang, Oxygen vacancy-mediated photocatalysis of BiOCl: reactivity, selectivity, and perspectives, *Angew. Chem., Int. Ed.*, 2018, 57, 122–138.
- 16 S. Xu, X. Chen, S. Zhan, S. Tian and Y. Xiong, Fe doped CeO₂ nanocubes with the exposure of active (100) facets for photocatalytic ozonation of 4-chlorophenol under solar irradiation, *J. Chem. Technol. Biotechnol.*, 2021, 96, 1523–1532.
- 17 J. Chen, S. Tian, J. Lu and Y. Xiong, Catalytic performance of MgO with different exposed crystal facets towards the

- ozonation of 4-chlorophenol, *Appl. Catal., A*, 2015, **506**, 118–125.
- 18 C. He, Y. Wang, Z. Li, Y. Huang, Y. Liao, D. Xia and S. Lee, Facet engineered α -MnO₂ for efficient catalytic ozonation of odor CH₃SH: oxygen vacancy-induced active centers and catalytic mechanism, *Environ. Sci. Technol.*, 2020, **54**, 12771–12783.
 - 19 T.-M. Tran-Thuy, T.-P. Tran and D. Van Nguyen, Cobalt-doped cryptomelane: surface-tailored oxygen defects and efficiently catalytic ozonation of p-Nitrophenol, *Top. Catal.*, 2022, **66**, 289–296.
 - 20 A. A. Esmailpour, J. Horlyck, P. Kumar, C. Tsounis, J. Yun, R. Amal and J. Scott, Engineering multidefects on Ce_xSi_{1-x}O_{2-δ} nanocomposites for the catalytic ozonation reaction, *Small*, 2022, **18**, e2103530.
 - 21 S. Afzal, X. Quan and S. Lu, Catalytic performance and an insight into the mechanism of CeO₂ nanocrystals with different exposed facets in catalytic ozonation of p-nitrophenol, *Appl. Catal., B*, 2019, **248**, 526–537.
 - 22 J. Yang, J. Xiao, H. Cao, Z. Guo, J. Rabeah, A. Bruckner and Y. Xie, The role of ozone and influence of band structure in WO₃ photocatalysis and ozone integrated process for pharmaceutical wastewater treatment, *J. Hazard. Mater.*, 2018, **360**, 481–489.
 - 23 A. Rey, E. Mena, A. M. Chávez, F. J. Beltrán and F. Medina, Influence of structural properties on the activity of WO₃ catalysts for visible light photocatalytic ozonation, *Chem. Eng. Sci.*, 2015, **126**, 80–90.
 - 24 X. Liu, Z. Guo, L. Zhou, J. Yang, H. Cao, M. Xiong, Y. Xie and G. Jia, Hierarchical biomimetic BiVO₄ for the treatment of pharmaceutical wastewater in visible-light photocatalytic ozonation, *Chemosphere*, 2019, **222**, 38–45.
 - 25 X. Chen, S. Zhan, D. Chen, C. He, S. Tian and Y. Xiong, Grey Fe-CeO_{2-σ} for boosting photocatalytic ozonation of refractory pollutants: Roles of surface and bulk oxygen vacancies, *Appl. Catal., B*, 2021, **286**, 119928.
 - 26 J. Lu, J. Sun, X. Chen, S. Tian, D. Chen, C. He and Y. Xiong, Efficient mineralization of aqueous antibiotics by simultaneous catalytic ozonation and photocatalysis using MgMnO₃ as a bifunctional catalyst, *Chem. Eng. J.*, 2019, **358**, 48–57.
 - 27 J. Kaur and S. Singhal, Facile synthesis of ZnO and transition metal doped ZnO nanoparticles for the photocatalytic degradation of Methyl Orange, *Ceram. Int.*, 2014, **40**, 7417–7424.
 - 28 J. Peng, T. Lu, H. Ming, Z. Ding, Z. Yu, J. Zhang and Y. Hou, Enhanced photocatalytic ozonation of phenol by Ag/ZnO nanocomposites, *Catalysts*, 2019, **9**, 1006.
 - 29 T. Yang, J. Peng, Y. Zheng, X. He, Y. Hou, L. Wu and X. Fu, Enhanced photocatalytic ozonation degradation of organic pollutants by ZnO modified TiO₂ nanocomposites, *Appl. Catal., B*, 2018, **221**, 223–234.
 - 30 G. Zhang, D. Chen, N. Li, Q. Xu, H. Li, J. He and J. Lu, Fabrication of Bi₂MoO₆/ZnO hierarchical heterostructures with enhanced visible-light photocatalytic activity, *Appl. Catal., B*, 2019, **250**, 313–324.
 - 31 J. Wang, Y. Xia, Y. Dong, R. Chen, L. Xiang and S. Komarneni, Defect-rich ZnO nanosheets of high surface area as an efficient visible-light photocatalyst, *Appl. Catal., B*, 2016, **192**, 8–16.
 - 32 Y. Chen, H. Zhao, B. Liu and H. Yang, Charge separation between wurtzite ZnO polar {001} surfaces and their enhanced photocatalytic activity, *Appl. Catal., B*, 2015, **163**, 189–197.
 - 33 G. Kresse and J. Furthmüller, Efficient iterative schemes for ab initio total-energy calculations using a plane-wave basis set, *Phys. Rev. B: Condens. Matter Mater. Phys.*, 1996, **54**, 11169–11186.
 - 34 G. Kresse and D. Joubert, From ultrasoft pseudopotentials to the projector augmented-wave method, *Phys. Rev. B: Condens. Matter Mater. Phys.*, 1999, **59**, 1758–1775.
 - 35 J. P. Perdew, K. Burke and M. Ernzerhof, Generalized Gradient Approximation Made Simple, *Phys. Rev. Lett.*, 1996, **77**, 3865–3868.
 - 36 Q. Wang, H. Zhou, X. Liu, T. Li, C. Jiang, W. Song and W. Chen, Facet-dependent generation of superoxide radical anions by ZnO nanomaterials under simulated solar light, *Environ. Sci.: Nano*, 2018, **5**, 2864–2875.
 - 37 Z. Li, M. A. Boda, X. Pan and Z. Yi, Photocatalytic oxidation of small molecular hydrocarbons over ZnO nanostructures: the difference between methane and ethylene and the impact of polar and nonpolar facets, *ACS Sustainable Chem. Eng.*, 2019, **7**, 19042–19049.
 - 38 M. Wang, Z. Shen, Y. Chen, Y. Zhang and H. Ji, Atomic structure-dominated enhancement of acetone sensing for a ZnO nanoplate with highly exposed (0001) facet, *CrystEngComm*, 2017, **19**, 6711–6718.
 - 39 K. Kim, P. G. Choi, T. Itoh and Y. Masuda, Effect of oxygen vacancy sites in exposed crystal facet on the gas sensing performance of ZnO nanomaterial, *J. Am. Ceram. Soc.*, 2021, **105**, 2150–2160.
 - 40 L. Niu, S. Hong and M. Wang, Properties of ZnO with oxygen vacancies and its application in humidity sensor, *J. Electron. Mater.*, 2021, **50**, 4480–4487.
 - 41 Y. Xu, H. Li, B. Sun, P. Qiao, L. Ren, G. Tian, B. Jiang, K. Pan and W. Zhou, Surface oxygen vacancy defect-promoted electron-hole separation for porous defective ZnO hexagonal plates and enhanced solar-driven photocatalytic performance, *Chem. Eng. J.*, 2020, **379**, 122295.
 - 42 C. Zhou, J. Shi, W. Zhou, K. Cheng, Q. Zhang, J. Kang and Y. Wang, Highly active ZnO-ZrO₂ aerogels integrated with H-ZSM-5 for aromatics synthesis from carbon dioxide, *ACS Catal.*, 2019, **10**, 302–310.
 - 43 S. Mehta and K. Joshi, From molecular adsorption to decomposition of methanol on various ZnO facets: a periodic DFT study, *Appl. Surf. Sci.*, 2022, **602**, 154150.
 - 44 V. Butera, Y. Tanabe, Y. Shinke, T. Miyazawa, T. Fujitani, M. Kayanuma and Y. K. Choe, Mechanistic investigation on ethanol-to-butadiene conversion reaction over metal oxide clusters, *Int. J. Quantum Chem.*, 2020, **121**, e26494.
 - 45 Y. Wang, S. Kattel, W. Gao, K. Li, P. Liu, J. G. Chen and H. Wang, Exploring the ternary interactions in Cu-ZnO-ZrO₂

- catalysts for efficient CO₂ hydrogenation to methanol, *Nat. Commun.*, 2019, **10**, 1166.
- 46 X. Nie, X. Ren, C. Tu, C. Song, X. Guo and J. G. Chen, Computational and experimental identification of strong synergy of the Fe/ZnO catalyst in promoting acetic acid synthesis from CH₄ and CO₂, *Chem. Commun.*, 2020, **56**, 3983–3986.
- 47 F. Gong, L. Peng, Y. Zhang, Y. Cao, D. Jia and F. Li, Selectively sensing H₂S and acetone through tailoring the facets exposed on the surfaces of ZnO supercrystals, *Mater. Lett.*, 2018, **218**, 106–109.
- 48 Y. Zhou, D. Zhao, L. Yang, Z. Zhao, D. Li, Q. Luo, Y. Zhang and F. Cao, Influences of graphene nanosheets coating on selectively exposed crystal facet ZnO, *ChemistrySelect*, 2018, **3**, 4495–4500.
- 49 M. R. Alenezi, S. J. Henley, N. G. Emerson and S. R. Silva, From 1D and 2D ZnO nanostructures to 3D hierarchical structures with enhanced gas sensing properties, *Nanoscale*, 2014, **6**, 235–247.
- 50 X. Li, Y. Tu, S. Pace, U. Anselmi-Tamburini and J. Briscoe, Influence of ZnO nanorod surface chemistry on passivation effect of TiO₂ shell coating, *J. Phys. D: Appl. Phys.*, 2021, **54**, 255107.
- 51 S. A. Ansari, M. M. Khan, S. Kalathil, A. Nisar, J. Lee and M. H. Cho, Oxygen vacancy induced band gap narrowing of ZnO nanostructures by an electrochemically active biofilm, *Nanoscale*, 2013, **5**, 9238–9246.
- 52 F. Kayaci, S. Vempati, I. Donmez, N. Biyikli and T. Uyar, Role of zinc interstitials and oxygen vacancies of ZnO in photocatalysis: a bottom-up approach to control defect density, *Nanoscale*, 2014, **6**, 10224–10234.
- 53 H. Ming, D. Wei, Y. Yang, B. Chen, C. Yang, J. Zhang and Y. Hou, Photocatalytic activation of peroxymonosulfate by carbon quantum dots functionalized carbon nitride for efficient degradation of bisphenol A under visible-light irradiation, *Chem. Eng. J.*, 2021, **424**, 130296.
- 54 Z. Lou, P. Wang, B. Huang, Y. Dai, X. Qin, X. Zhang, Z. Wang and Y. Liu, Enhancing charge separation in photocatalysts with internal polar electric fields, *ChemPhotoChem*, 2017, **1**, 136–147.
- 55 K. He, Y. Dong, L. Yin, A. Zhang and Z. Li, A facile hydrothermal method to synthesize nanosized Co₃O₄/CeO₂ and study of its catalytic characteristic in catalytic ozonation of phenol, *Catal. Lett.*, 2009, **133**, 209–213.
- 56 Q. Y. Wu, Z. W. Yang, Y. Du, W. Y. Ouyang and W. L. Wang, The promotions on radical formation and micropollutant degradation by the synergies between ozone and chemical reagents (synergistic ozonation): a review, *J. Hazard. Mater.*, 2021, **418**, 126327.
- 57 E. Asgari, A. Sheikhmohammadi, H. Nourmoradi, S. Nazari and M. Aghanaghad, Degradation of ciprofloxacin by photocatalytic ozonation process under irradiation with UVA: comparative study, performance and mechanism, *Process Saf. Environ. Prot.*, 2021, **147**, 356–366.
- 58 H. Guo, H. Yang, J. Huang, J. Tong, X. Liu, Y. Wang, W. Qiao and J. Han, Theoretical and experimental insight into plasma-catalytic degradation of aqueous p-nitrophenol with graphene-ZnO nanoparticles, *Sep. Purif. Technol.*, 2022, **295**, 121362.
- 59 G. Yu, Y. Wang, H. Cao, H. Zhao and Y. Xie, Reactive oxygen species and catalytic active sites in heterogeneous catalytic ozonation for water purification, *Environ. Sci. Technol.*, 2020, **54**, 5931–5946.
- 60 J. Yao, Z. Chen, H. Zhang, N. Gao, Z. Zhang and W. Jiang, New insight into the regulation mechanism of visible light in naproxen degradation via activation of peroxymonosulfate by MOF derived BiFeO₃, *J. Hazard. Mater.*, 2022, **431**, 128513.